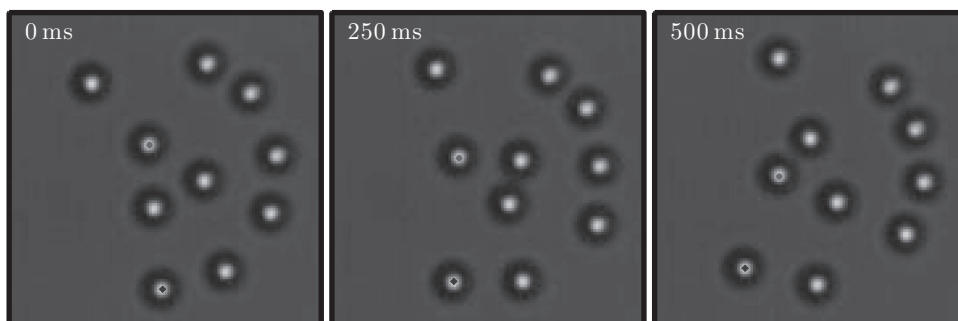


The most basic optical tweezers set-up, e.g., the one we built in Chapter 8, produces a *single* optical trap by focusing a *single* optical beam. By using more than one beam, or by splitting a single beam, it is possible to generate multiple traps. This procedure, however, leads to rather complex, and sometimes messy, set-ups. Additionally, to steer these traps it is necessary to move some mechanical components of the optical set-up. Finally, using non-Gaussian beams demands the use of specialised optical components, e.g., axicons to generate Bessel beams or holographic masks to generate higher-order Laguerre–Gaussian beams. To overcome these difficulties, it is possible to employ *holographic optical tweezers* (HOTs). HOTs use a computer-controlled diffractive optical element (DOE) to split a single collimated laser beam into several separate beams, each of which is focused into an optical tweezers. These optical traps can be made dynamic and displaced in three dimensions by projecting a sequence of holograms and, furthermore, non-Gaussian beam profiles can be straightforwardly encoded in the holographic mask, such as the Laguerre–Gaussian beams employed in the optical trapping experiment shown in Fig. 11.1. In this chapter, we explain how to design and operate HOTs.



**Figure 11.1**

Rotating particles in Laguerre–Gaussian beams. Particles (polystyrene, 1  $\mu\text{m}$  radius) trapped in two concentric Laguerre–Gaussian beams with opposite helicity: the particles in the outer ring are pushed clockwise by a Laguerre–Gaussian beam with helicity  $+40$ , while the ones in the inner ring are pushed anticlockwise (at a faster angular speed) by a Laguerre–Gaussian beam with helicity  $-10$ . The particles are confined in a quasi-two-dimensional space by the scattering force that pushes them against the upper coverslip of the sample chamber.

\* This chapter was written together with Giuseppe Pesce.

## 11.1 Basic working principle

The basic working principle of HOTs is shown in Fig. 11.2. A DOE is employed to shape the profile of an incoming optical beam, which for simplicity we assume to have uniform intensity and, more importantly, uniform phase. The DOE is positioned at the front focal plane of the Fourier lens (to which we will refer from now on as the *DOE plane*), which collects the first-order diffracted beam, so that the complex amplitude in the back focal plane

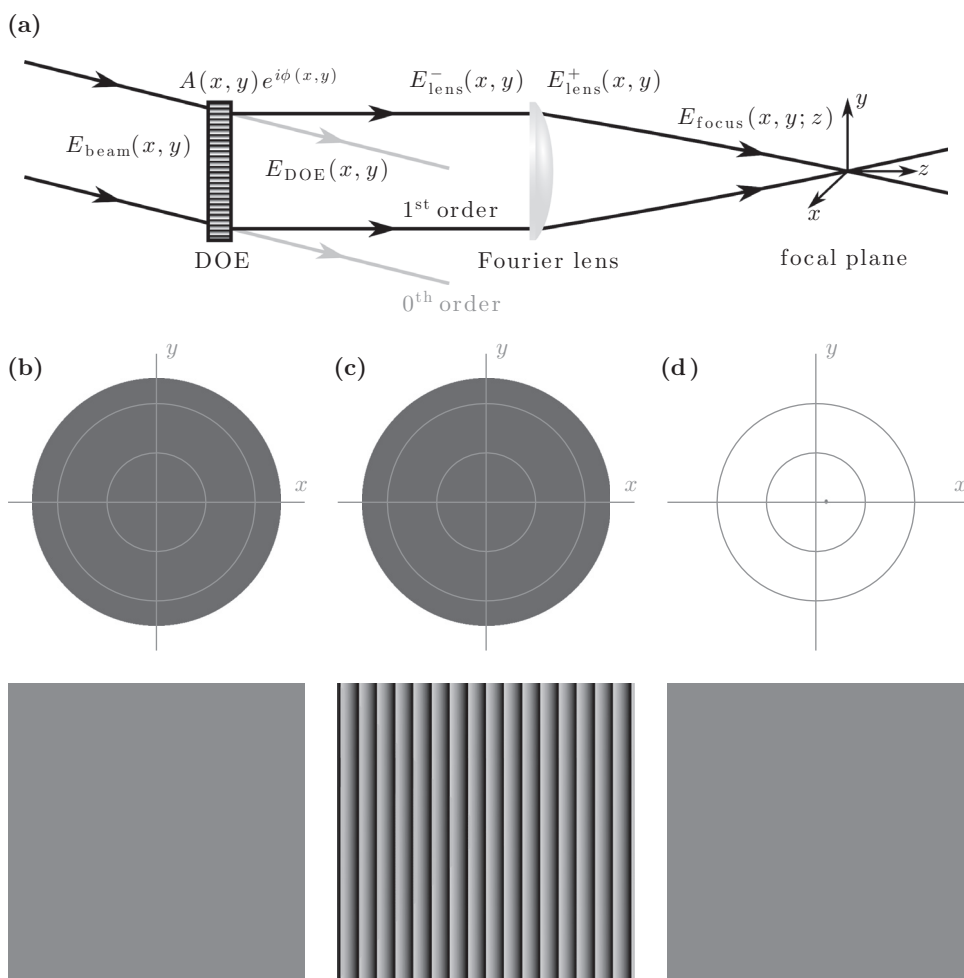


**Figure 11.2** HOT working principle. (a) A diffractive optical element (DOE) alters the beam profile of an incoming optical beam (with uniform intensity and phase). The DOE is positioned in the front focal plane of the Fourier lens (the DOE plane), which collects the first-order diffracted beam, so that the complex amplitude in the back focal plane of the Fourier lens (the focal plane) is the Fourier transform of the complex amplitude in the DOE plane. Intensity (top) and phase (bottom) profiles of (b) the incoming beam, (c) the beam after the DOE and (d) the focused beam at the focal plane.

## Box 11.1

## Fresnel diffraction integral

Given the electromagnetic field  $E(x, y; 0)$  defined in the plane  $z = 0$ , the field  $E(x, y; z)$  in the plane  $z = \text{constant}$  can be calculated using the *Fresnel diffraction integral*, i.e.,

$$E(x, y; z) = \frac{e^{ik_0 z}}{i\lambda_0 z} \iint_{-\infty}^{+\infty} E(x', y'; 0) e^{i\frac{k_0}{2z}[(x-x')^2 + (y-y')^2]} dx' dy',$$

where  $k_0$  and  $\lambda_0$  are the vacuum wavenumber and wavelength. This integral is the convolution

$$E(x, y, z) = h(x, y, z) * E(x, y, 0),$$

where

$$h(x, y, z) = \frac{e^{ik_0 z}}{i\lambda_0 z} e^{i\frac{k_0}{2z}[x^2 + y^2]}$$

is the *impulse response* of free space propagation. Taking the two-dimensional Fourier transform, we obtain its expression in the frequency domain,

$$\check{E}(f_x, f_y; z) = \check{H}(f_x, f_y; z) \check{E}(f_x, f_y; 0),$$

where  $f_x = \lambda_0^{-1}x/z$  and  $f_y = \lambda_0^{-1}y/z$  are the spatial frequencies,  $\check{E}(f_x, f_y; z)$  is the Fourier transform of  $E(x, y; z)$ ,  $\check{E}(f_x, f_y; 0)$  is the Fourier transform of  $E(x, y; 0)$  and

$$\check{H}(f_x, f_y; z) = e^{ik_0 z} e^{-i\pi\lambda z[f_x^2 + f_y^2]}$$

is the Fourier transform of the impulse response multiplied by  $4\pi^2$  (this factor can also be  $1$  or  $2\pi$  depending on the convention used to define the Fourier transform).

plane of the Fourier lens (from now on the *focal plane*) is the Fourier transform of the complex amplitude at the DOE plane.

We will now make these considerations more quantitative. We consider an incoming paraxial beam with transverse profile  $E_{\text{beam}}(x, y)$ . The effect of the DOE is to alter the beam profile by a complex factor  $A(x, y)e^{i\phi(x, y)}$ , where  $A(x, y)$  is a (real) intensity attenuation factor and  $\phi(x, y)$  is a phase factor. Therefore, the electric field just after the DOE is

$$E_{\text{DOE}}(x, y) = A(x, y)e^{i\phi(x, y)}E_{\text{beam}}(x, y). \quad (11.1)$$

We can now propagate  $E_{\text{DOE}}(x, y)$  from the DOE plane up to the entrance pupil of the lens using the Fresnel diffraction integral [Box 11.1], obtaining

$$E_{\text{lens}}^-(x, y) = \frac{e^{ik_0 f}}{i\lambda_0 f} e^{i\frac{k_0}{2f}[x^2 + y^2]} \iint_{-\infty}^{+\infty} E_{\text{DOE}}(x', y') e^{i\frac{k_0}{2f}[x'^2 + y'^2]} e^{-i\frac{2\pi}{\lambda_0 f}[xx' + yy']} dx' dy', \quad (11.2)$$

where  $k_0$  is the vacuum wavenumber,  $\lambda_0$  is the vacuum wavelength,  $f$  is the focal distance of the lens and the superscript ‘ $-$ ’ indicates that we consider the beam just *before* the lens.

Within the thin lens approximation and assuming the diameter of the lens to be significantly larger than the size of the beam, the effect of the Fourier lens is to add a quadratic phase factor to the beam profile, i.e.,

$$E_{\text{lens}}^+(x, y) = E_{\text{lens}}^-(x, y)e^{-i\frac{k_0}{2f}[x^2+y^2]}, \quad (11.3)$$

where the superscript ‘+’ indicates that we consider the beam just *after* the lens,<sup>1</sup> so that

$$E_{\text{lens}}^+(x, y) = \frac{e^{ik_0f}}{i\lambda_0f} \iint_{-\infty}^{+\infty} E_{\text{DOE}}(x', y')e^{i\frac{k_0}{2f}[x'^2+y'^2]}e^{-i\frac{2\pi}{\lambda_0f}[xx'+yy']}dx'dy'. \quad (11.4)$$

At this point, we apply the Fresnel diffraction formula to propagate  $E_{\text{lens}}^+(x, y)$  from the lens exit pupil to its focal plane, obtaining

$$E_{\text{focus}}(x, y) = \frac{e^{ik_0f}}{i\lambda_0f}e^{i\frac{k_0}{2f}[x^2+y^2]} \iint_{-\infty}^{+\infty} E_{\text{lens}}^+(x', y')e^{i\frac{k_0}{2f}[x'^2+y'^2]}e^{-i\frac{2\pi}{\lambda_0f}[xx'+yy']}dx'dy'. \quad (11.5)$$

By substituting Eq. (11.3) into Eq. (11.5), we obtain

$$E_{\text{focus}}(x, y) = \frac{e^{ik_0f}}{i\lambda_0f}e^{i\frac{k_0}{2f}[x^2+y^2]}4\pi^2\check{E}_{\text{lens}}^-(f_x, f_y), \quad (11.6)$$

where  $f_x = \lambda_0^{-1}x/f$ ,  $f_y = \lambda_0^{-1}y/f$  and

$$\check{E}_{\text{lens}}(f_x, f_y) = \frac{1}{4\pi^2} \iint_{-\infty}^{+\infty} E_{\text{lens}}^-(x, y)e^{-i2\pi[f_x x + f_y y]}dxdy \quad (11.7)$$

is the Fourier transform of  $E_{\text{lens}}^-(x, y)$ .

Finally, we can substitute the Fourier transform of Eq. (11.2) [Box 11.1], i.e.,

$$\check{E}_{\text{lens}}^-(f_x, f_y) = e^{ik_0z}e^{-i\pi\lambda z[f_x^2+f_y^2]}\check{E}_{\text{DOE}}(f_x, f_y), \quad (11.8)$$

into Eq. (11.6) to derive the expression relating the field at the DOE plane and at the focal plane,

$$E_{\text{focus}}(x, y) = \frac{e^{2ik_0f}}{i\lambda_0f}4\pi^2\check{E}_{\text{DOE}}(f_x, f_y). \quad (11.9)$$

As anticipated at the beginning of this section, Eq. (11.9) shows that the field in the focal plane of the lens is the Fourier transform of the field at the DOE plane. This means that the field at a certain position in the focal plane is proportional to the amplitude of a certain spatial frequency in the DOE plane.

<sup>1</sup> To be precise, a constant phase factor of the form  $e^{ik_0n_1\Delta l}$  should also be considered, where  $n_1$  is the lens refractive index and  $\Delta l$  is the lens central thickness. However, this becomes relevant only if interferometric measurement is considered, so that it can be safely ignored in our case.

**Exercise 11.1.1** Show that, if (as is often the case) the input beam can be modelled with a plane wave, i.e.,  $E_{\text{beam}}(x, y) \equiv E_0$ , the field in the focal plane is determined solely by the profile imposed by the DOE. What happens if the incoming field is a Gaussian beam? And if it is a Laguerre–Gaussian beam?

**Exercise 11.1.2** Show that the effect of a blazed grating on the DOE, e.g., along the  $x$ -direction, is to deflect the impinging beam (assume it to have a constant phase and amplitude) by an angle

$$\alpha_x \approx \tan \alpha_x = \frac{\lambda_0}{\Lambda_x}, \quad (11.10)$$

where  $\Lambda_x$  is the periodicity of the grating. This is typically a small angle, at most about  $1^\circ$ . How much is it for the case when  $\lambda_0 = 1064 \text{ nm}$  and the pixel size of the DOE  $d = 12 \mu\text{m}$ ? Show that such a blazed grating produces a displacement of the intensity spot at the front focal plane equal to

$$\Delta x = f \frac{\lambda_0}{\Lambda_x}. \quad (11.11)$$

Repeat the same analysis for a blazed grating along the  $y$ -direction and show that the sum of gratings along the  $x$ - and  $y$ -directions results in a grating that produces a diagonal shift equal to the combination of their shifts; i.e., the effects of gratings are additive.

**Exercise 11.1.3** Show that the relation between the field at the DOE plane and the field at planes different from (but close to) the focal plane is

$$E_{\text{focus}}(x, y; z) = \frac{e^{ik_0[2f+z]} e^{ik_0[x^2+y^2]}}{i\lambda_0 f} 4\pi^2 \check{E}_{\text{DOE},z}(f_x, f_y), \quad (11.12)$$

where  $\check{E}_{\text{DOE},z}(f_x, f_y)$  is the Fourier transform of

$$E_{\text{DOE}}(x, y) e^{-i \frac{\pi z}{\lambda_0 f^2} [x^2+y^2]}. \quad (11.13)$$

Note that the term  $e^{-i \frac{\pi z}{\lambda_0 f^2} [x^2+y^2]}$  represents the phase of a *Fresnel lens*, whose role is to alter the curvature of the incoming beam (see also the following exercise).

**Exercise 11.1.4** Show that the effect of imposing a Fresnel lens on the DOE is to alter the curvature of the incoming beam (assume it to have a constant phase and amplitude) and that, if the Fresnel lens focal length is  $f_F$ , the intensity spot at the front focal plane is displaced along the  $z$ -direction by

$$\Delta z = \frac{f^2}{f_F}. \quad (11.14)$$

**Exercise 11.1.5** Show that imposing on the DOE a phase profile corresponding to the sum of a grating and a Fresnel lens results in a displacement of the focal spot in the lateral and axial directions, corresponding respectively to the effect of the grating and of the Fresnel lens.

## 11.2 Computer-generated holograms

In optical trapping and manipulation applications, point traps, higher-order beams and continuous intensity distributions for the desired trapping pattern are typically employed. In principle, given a desired intensity distribution in the front focal plane, it is sufficient to take its inverse Fourier transform to determine the appropriate hologram to place on the DOE. However, the result of this simple operation is typically a hologram that modulates both the phase and the amplitude of the input beam. On one hand, employing such a hologram would require modulating both the phase and the amplitude of the incoming laser beam. On the other hand, amplitude modulation would remove power from the beam, leading to significantly reduced efficiency. Therefore, it is usually more convenient to employ a phase-only hologram.

In the following, we will consider the incoming beam to be a uniform plane wave, i.e.,  $E_{\text{beam}}(x, y) \equiv E_0$ . The DOE is typically a two-dimensional pixellated device whose pixels have area  $d^2$ , row index  $m_x = 1, \dots, M_x$  and column index  $m_y = 1, \dots, M_y$ . The complex amplitude imposed on the incoming beam by pixel  $[m_x, m_y]$  is  $A_{m_x, m_y} = A \exp\{i\phi_{m_x, m_y}\}$ , where  $A$  is a (real) attenuation constant and  $\phi_{m_x, m_y}$  is a phase shift. Therefore, the electric field after the DOE is  $E_{m_x, m_y} = A \exp\{i\phi_{m_x, m_y}\} E_0$ . From Eq. (11.12), we can now calculate the electric field in the trap volume around the focal plane of the objective as

$$E_{\text{focus}}(x, y, z) = \frac{e^{i\frac{2\pi}{\lambda_0}[2f+z]} e^{i\frac{\pi}{\lambda_0 z}[x^2+y^2]}}{i\lambda_0 f} d^2 \sum_{m_x=1}^{M_x} \sum_{m_y=1}^{M_y} |E_0|^2 A^2 e^{i[\phi_{m_x, m_y} - \Delta_{m_x, m_y}(x, y, z)]}, \quad (11.15)$$

where

$$\Delta_{m_x, m_y}(x, y, z) = \frac{2\pi}{\lambda_0 f} [x_{m_x, m_y} x + y_{m_x, m_y} y] + \frac{\pi z}{\lambda_0 f^2} [x_{m_x, m_y}^2 + y_{m_x, m_y}^2] \quad (11.16)$$

and  $[x_{m_x, m_y}, y_{m_x, m_y}]$  are the pixels' coordinates.

We can now consider how much laser power flows through a diffraction-limited area around the position  $[x, y, z]$  within the trapping volume. The power, i.e., the total time-averaged energy flux, just after the DOE is

$$P_t = \frac{c\epsilon_0^2}{2} M_x M_y d^2 |E_0|^2 A^2. \quad (11.17)$$

The energy flux flowing through a diffraction-limited spot with area  $f^2 \lambda_0^2 / (M_x M_y d^2)$ , around position  $[x, y, z]$  is

$$P(x, y, z) = \frac{c\epsilon_0}{2} \frac{f^2 \lambda_0^2}{M_x M_y d^2} \frac{d^4}{\lambda_0^2 f^2} |E_0|^2 A^2 \left| \sum_{m_x=1}^{M_x} \sum_{m_y=1}^{M_y} e^{i(\phi_{m_x, m_y} - \Delta_{m_x, m_y}(x, y, z))} \right|^2. \quad (11.18)$$

Therefore, we can introduce the dimensionless variable

$$V(x, y, z) = \frac{1}{M_x M_y} \sum_{m_x=1}^{M_x} \sum_{m_y=1}^{M_y} e^{i(\phi_{m_x, m_y} - \Delta_{m_x, m_y}(x, y, z))}, \quad (11.19)$$

which is characterised by the property that

$$|V(x, y, z)|^2 = \frac{P(x, y, z)}{P_t} \quad (11.20)$$

and for  $z = 0$  corresponds to the discrete Fourier transform of  $\phi_{m_x, m_y}$  evaluated at the spatial frequencies  $[\lambda_0^{-1}x/f, \lambda_0^{-1}y/f]$ .

In the following subsections, our task will be to optimise the values of  $\phi_{m_x, m_y}$  imposed on the DOE in order to maximise the modulus of  $V(x, y, z)$  at some trapping sites, which are located at  $[x_{\text{ot},n}, y_{\text{ot},n}, z_{\text{ot},n}]$  for  $n = 1, \dots, N$ . We will focus our attention on standard Gaussian optical traps, whereas we consider higher-order beams in Section 11.3 and continuous optical potentials in Section 11.4.

### 11.2.1 Single steerable trap

The simplest case is a single trap, i.e.,  $N = 1$ , placed at  $[x_{\text{ot},1}, y_{\text{ot},1}, z_{\text{ot},1}]$ . The optimal phase modulation is immediately found to be

$$\phi_{m_x, m_y}^S(x_{\text{ot},1}, y_{\text{ot},1}, z_{\text{ot},1}) = \Delta_{m_x, m_y}(x_{\text{ot},1}, y_{\text{ot},1}, z_{\text{ot},1}), \quad (11.21)$$

for which  $V(x_{\text{ot},1}, y_{\text{ot},1}, z_{\text{ot},1}) = 1$ ; i.e., all the diffracted power is deflected into the trap. Thus,

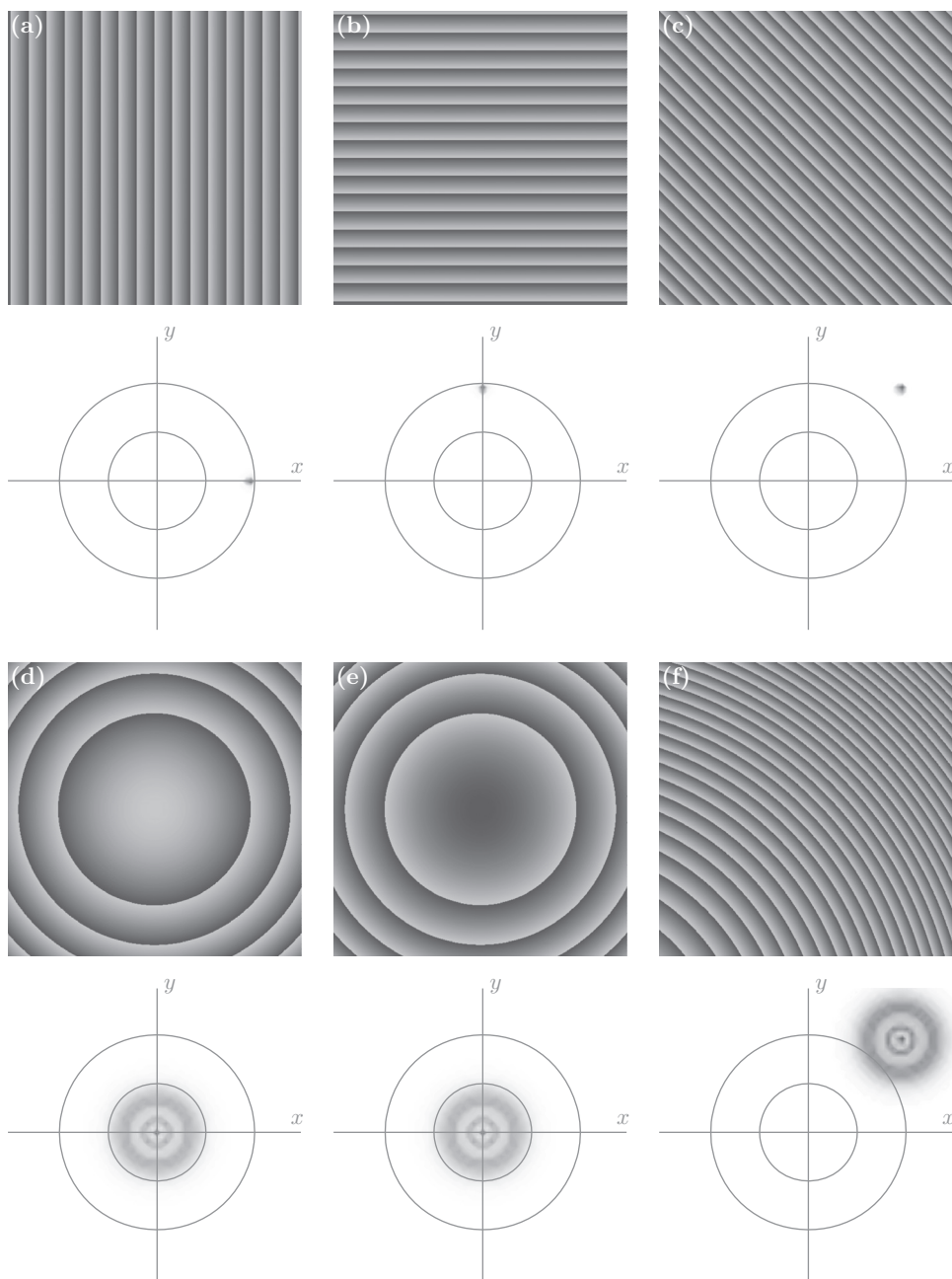
$$\phi_{m_x, m_y}^S = \underbrace{\frac{2\pi}{\lambda_0 f} [x_{m_x, m_y} x_{\text{ot},1} + y_{m_x, m_y} y_{\text{ot},1}]}_{\text{Diffraction grating}} + \underbrace{\frac{\pi z_{\text{ot},1}}{\lambda_0 f^2} [x_{m_x, m_y}^2 + y_{m_x, m_y}^2]}_{\text{Fresnel lens}}, \quad (11.22)$$

where the first term gives rise to a *blazed diffraction grating* phase pattern shifting the spot laterally [Figs. 11.3a, 11.3b and 11.3c], and the second term generates a phase retardation that is comparable to that of a *Fresnel lens* [Figs. 11.3d and 11.3e], shifting the spot along the axial direction. A combination of the two produces a shift of the trap in three dimensions [Fig. 11.3f]. Because the generation of the holographic mask given by Eq. (11.22) is computationally very fast, this is a very effective way to generate a single optical trap that can be moved in three dimensions in real time.

**Exercise 11.2.1** Simulate the intensity profile in the focal plane generated by a phase profile such as the one in Eq. (11.22). What happens when the parameters of the grating and of the Fresnel lens are changed? In particular, study the case of a grating made of alternating rows of pixels with phase  $0^\circ$  and  $180^\circ$  and note that the resulting intensity profile produces two symmetric spots. Why is this so? [Hint: You can adapt the program `s1m` from the book website.]

**Exercise 11.2.2** Show that any optical field in the focal plane can be shifted laterally by adding a diffraction grating phase profile to the hologram.

**Exercise 11.2.3** Show that any optical field in the focal plane can be shifted axially by adding a Fresnel lens phase profile to the hologram.

**Figure 11.3**

Gratings and Fresnel lenses. A single focal spot can be generated in the front focal plane of a lens by a phase modulation corresponding to a grating and/or a Fresnel lens: (a) grating along  $x$ ; (b) grating along  $y$ ; (c) combination of gratings along  $x$  and  $y$ ; (d) positive Fresnel lens; (e) negative Fresnel lens; (f) combination of the grating in (c) and Fresnel lens in (d). Both the phase modulation (top) and the focal spot intensity (bottom) are shown.



### 11.2.2 Random mask encoding

To generate multiple traps, i.e.,  $N > 1$ , one of the fastest, but also least efficient, algorithms is the *random mask encoding* algorithm. For every pixel of the SLM, a phase shift is determined as if the hologram was made to generate only one of the  $N$  traps, i.e.,

$$\phi_{m_x, m_y}^{\text{RM}} = \phi_{m_x, m_y}^{\text{S}}(x_{\text{ot}, n(m_x, m_y)}, y_{\text{ot}, n(m_x, m_y)}, z_{\text{ot}, n(m_x, m_y)}), \quad (11.23)$$

where  $\phi_{m_x, m_y}^{\text{S}}$  is given by Eq. (11.22) and  $n(m_x, m_y) \in [1, \dots, N]$  is chosen randomly for each pixel. This technique is very fast and permits one to achieve good uniformity amongst traps. Nevertheless, the overall efficiency can be very low when  $N$  is large, because on the average only  $M_x M_y / N$  pixels interfere constructively to generate each trap.

In order to quantify the performance of this algorithm and to benchmark it against the other algorithms we present in the following subsections, we test all algorithms against a standard task of computing a  $1000 \times 1000$  hologram for the generation of  $N = 100$  traps arranged on a  $10 \times 10$  square lattice located in the focal plane ( $z = 0$ ). Their performance is quantified by four parameters, *efficiency*,

$$I_{\text{tot}} = \sum_{n=1}^N I_n, \quad (11.24)$$

*average intensity*,

$$\langle I \rangle = \frac{I_{\text{tot}}}{N}, \quad (11.25)$$

*uniformity*,

$$u = 1 - \frac{\max[I_n] - \min[I_n]}{\max[I_n] + \min[I_n]} \quad (11.26)$$

and *percentage standard error*,

$$\sigma = \frac{\sqrt{\sum_{n=1}^N (I_n - \langle I \rangle)^2}}{N \langle I \rangle} \times 100, \quad (11.27)$$

where  $I_n$  is the intensity of the  $n$ th trap. As shown in Table 11.1, the random mask encoding obtains an efficiency  $I_{\text{tot}} = 0.01 \approx 1/N$ , which is quite low, as each trap has only an intensity  $\langle I \rangle = 0.0001 \approx 1/M^2$ , whereas the uniformity is quite good at  $u = 0.67$ .

**Exercise 11.2.4** Simulate the intensity profile in the focal plane generated by a phase profile such as the one in Eq. (11.23). Study how the efficiency [Eq. (11.24)] and the uniformity [Eq. (11.26)] of the trap array change as a function of its parameters. [Hint: You can adapt the program `slm` from the book website.]

**Exercise 11.2.5** Show how the random mask encoding algorithm can be quite efficient at generating some helper tweezers on top of a complex light structure obtained via a precalculated hologram using temporarily a fraction of the SLM pixels. Simulate the generation and use of helper tweezers numerically.

**Table 11.1** Comparison of algorithms to generate holograms

Algorithm <sup>a</sup>	$I_{\text{tot}}$ <sup>b</sup>	$u$ <sup>c</sup>	$\sigma$ <sup>d</sup>	$T_{\text{comp}}$ <sup>e</sup>
Random mask encoding	0.01	0.67	0.14	0.3 s
Superposition of gratings and lenses	0.29	0.007	2.59	4.6 s
Superposition of gratings and lenses with additional random phase	0.84	0.18	0.37	4.6 s
Gerchberg–Saxton algorithm	0.93	0.33	0.27	316 s
Adaptive-additive algorithm	0.93	0.99	0.0062	348 s

<sup>a</sup> All algorithms are tested against a standard task of computing a  $1000 \times 1000$  hologram for the generation of  $N = 100$  traps arranged on a  $10 \times 10$  square lattice located in the focal plane ( $z = 0$ ).

<sup>b</sup> Efficiency given by Eq. (11.24).

<sup>c</sup> Uniformity given by Eq. (11.26).

<sup>d</sup> Percentage standard error given by Eq. (11.27).

<sup>e</sup> Computational time on a standard laptop computer.

**Exercise 11.2.6** Show that the random mask encoding algorithm can be adapted to the generation of arrays of weighted traps by randomly assigning the available SLM pixels to the individual traps proportionally to the ratio of the square roots of the desired trap intensities. Study numerically the performance of the resulting algorithm. [Hint: You can adapt the program `slm` from the book website.]

### 11.2.3 Superposition of gratings and lenses

Another straightforward algorithm, which achieves a better efficiency than the random mask encoding at a just slightly higher computational cost, is the *superposition of gratings and lenses* algorithm. In this algorithm, the phase of each pixel is chosen to be equal to the argument of the complex sum of single-trap holograms given by Eq. (11.22), i.e.,

$$\phi_{m_x, m_y}^{\text{SGL}} = \arg \left\{ \sum_{n=1}^N e^{i\phi_{m_x, m_y}^S(x_{\text{ot}, n}, y_{\text{ot}, n}, z_{\text{ot}, n})} \right\}. \quad (11.28)$$

This algorithm typically has good efficiency at the cost of poor uniformity. For example, in the benchmark test we present in Table 11.1, we obtained  $I_{\text{tot}} = 0.29$  and  $u = 0.007$ . A typical problem that arises using this algorithm is that, when highly symmetrical trap geometries are sought, such as the one of our benchmark, a consistent part of the energy is diverted to unwanted ghost traps.<sup>2</sup>

<sup>2</sup> If the precise location of the traps is not crucial, it might be useful to add some small amount of noise to the location of each trap in order to improve the array uniformity.

**Exercise 11.2.7** Simulate the intensity profile in the focal plane generated by a hologram obtained from the superposition of gratings and lenses [Eq. (11.28)]. Study how the efficiency [Eq. (11.24)] and the uniformity [Eq. (11.26)] of the trap array change as a function of its parameters. [Hint: You can adapt the program `s1m` from the book website.]

**Exercise 11.2.8** Show that the superposition of gratings and lenses [Eq. (11.28)] results from the maximisation of

$$\sum_{n=1}^N \operatorname{Re} \{ V(x_{\text{ot},n}, y_{\text{ot},n}, z_{\text{ot},n}) \},$$

with respect to the arguments  $\phi_{m_x, m_y}$ , i.e., it maximises the sum of the projections of the  $V(x_{\text{ot},n}, y_{\text{ot},n}, z_{\text{ot},n})$  [Eq. (11.19)] along the real axis of the complex plane. [Hint: Impose the vanishing of the first derivative with respect to  $\phi_{m_x, m_y}$  to find the stationary solutions and, then, identify the local maxima imposing that the Hessian matrix is negative definite.]

**Exercise 11.2.9** Show that the efficiency of the superposition of gratings and lenses algorithm can be improved by adding a random phase to each single-trap hologram, i.e.,

$$\phi_{m_x, m_y}^{\text{SGL}} = \arg \left\{ \sum_{n=1}^N e^{i\phi_{m_x, m_y}^S(x_{\text{ot},n}, y_{\text{ot},n}, z_{\text{ot},n} + \theta_n)} \right\}, \quad (11.29)$$

where  $\theta_n$  are random phases. This algorithm is known as *random superposition of gratings and lenses*. Show that this algorithm corresponds to maximising the sum of the amplitudes of  $V(x_{\text{ot},n}, y_{\text{ot},n}, z_{\text{ot},n})$  [Eq. (11.19)] projected on a randomly chosen direction in the complex plane, i.e., to maximising

$$\sum_{n=1}^N \operatorname{Re} \{ V(x_{\text{ot},n}, y_{\text{ot},n}, z_{\text{ot},n}) e^{-i\theta_n} \}.$$

**Exercise 11.2.10** Show that an array of weighted traps can be generated by weighting the terms of the sum in Eq. (11.28) by the square roots of the desired trap intensities. Verify the result numerically. [Hint: You can adapt the program `s1m` from the book website.]

### 11.2.4 Gerchberg–Saxton algorithm

The *Gerchberg–Saxton algorithm* was originally developed by Gerchberg and Saxton (1972) for crystallographic applications. The basic idea is illustrated in Fig. 11.4: it is an iterative algorithm that permits one to find a phase distribution that turns a given input intensity distribution arriving at the DOE plane into a desired intensity distribution in the trapping plane by propagating the complex amplitude back and forth between these two planes and replacing at each step the intensity on the trapping plane with the target intensity and that on the DOE plane with the laser's actual intensity profile. It typically converges after a few tens of iterations; for example, in the benchmark test we present in Table 11.1, we obtained

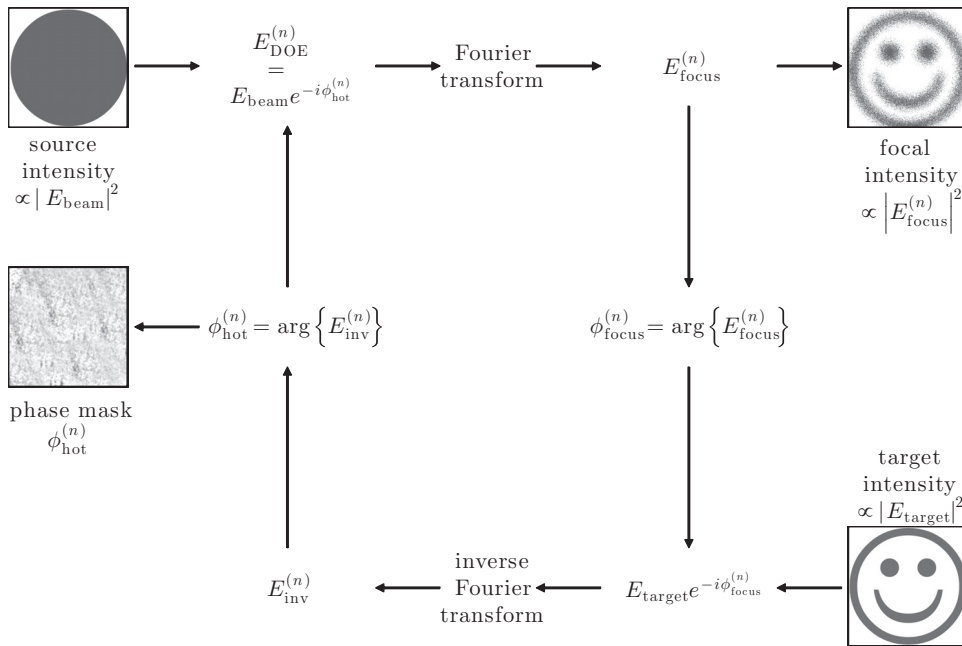


Figure 11.4

The Gerchberg–Saxton algorithm. Given the incoming beam electric field  $E_{\text{beam}}$ , the Gerchberg–Saxton algorithm permits one to obtain a phase distribution for the hologram at the DOE plane  $\phi_{\text{hot}}$  that permits one to approximate the target intensity distribution at the focal plane. At the  $n$ th iteration of the algorithm, the amplitude of the field at the DOE,  $E_{\text{DOE}}^{(n)}$ , is given by  $E_{\text{beam}}$  and its phase by  $\phi_{\text{hot}}^{(n)}$ . The focal field  $E_{\text{focus}}^{(n)}$  is given by the Fourier transform of  $E_{\text{DOE}}^{(n)}$ . Next, the amplitude of the focal field is substituted with the target intensity amplitude and the resulting field is inverse Fourier transformed, obtaining  $E_{\text{inv}}^{(n)}$ . Finally, the hologram phase is updated to the phase of  $E_{\text{inv}}^{(n)}$ . If the focal intensity and the target intensity differ more than an acceptable error, the cycle is then repeated (until a certain maximum number of iterations is reached).

$I_{\text{tot}} = 0.93$  and  $u = 0.33$  after 30 iterations. This algorithm is ideally suited to deal with continuous intensity distributions, as we will see in more detail in Section 11.4.

**Exercise 11.2.11** Implement the Gerchberg–Saxton algorithm and study its performance.

**Exercise 11.2.12** Noting that, when the target intensity is an array of point traps, it is unnecessary to calculate the field complex amplitude in points whose amplitude will be replaced by zero before back-propagation, propose an alternative (more efficient) implementation of the Gerchberg–Saxton algorithm where the field is computed only at the trap locations.

**Exercise 11.2.13** Show that the uniformity of the resulting trap array can be improved by aiming at a slightly modified target intensity distribution. [Hint: At each iteration, adjust the target intensity profile in order to reduce deviations from the average intensity. This algorithm is known as the *weighted Gerchberg–Saxton algorithm*.]

**Exercise 11.2.14** Extend the Gerchberg–Saxton algorithm to three-dimensional trapping geometries by considering multiple planes for forward propagation and obtaining the

back-propagated field as the complex sum of the corrected and back-propagated fields from the target planes. Then, proceed to generalise the Gerchberg–Saxton algorithm to full three-dimensional shaping.

### 11.2.5 Adaptive–additive algorithm

An alternative iterative approach is the *adaptive-additive algorithm*, which was first applied to the generation of holographic optical trap arrays by Dufresne et al. (2001). The basic idea of this algorithm is presented in Fig. 11.5: starting with an arbitrary guess of the phase profile and an initial input wavefront, the Fourier transform of this wavefront is the starting estimate for the output electric field; the resulting error in the focal plane is reduced by mixing a proportion,  $a$ , of the desired amplitude into the field in the focal plane; inverse-Fourier transforming the resulting focal field yields the corresponding field in the input plane; the amplitude in the input plane is replaced with the actual amplitude of the laser profile; finally, the algorithm is iterated. The main advantage of this algorithm in comparison to the Gerchberg–Saxton algorithm is that it permits one to achieve better

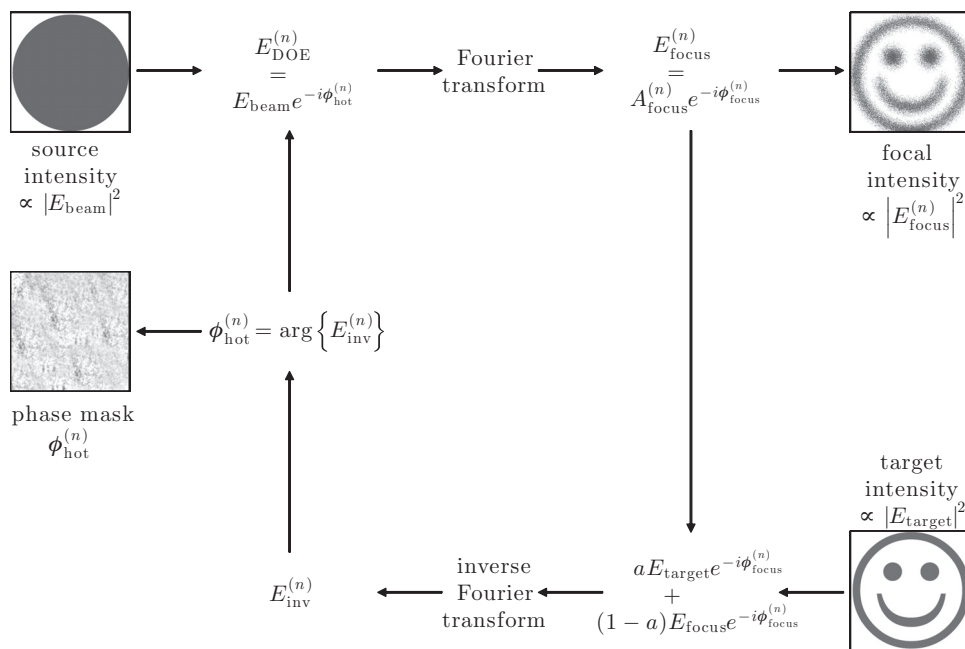


**Figure 11.5** The adaptive–additive algorithm. The algorithm is quite similar to the Gerchberg–Saxton algorithm illustrated in Fig. 11.4. At the  $n$ th iteration, the amplitude of the field at the DOE,  $E_{\text{DOE}}^{(n)}$ , is given by  $E_{\text{beam}}$  and its phase by  $\phi_{\text{hot}}^{(n)}$ . The focal field  $E_{\text{focus}}^{(n)}$  is given by the Fourier transform of  $E_{\text{DOE}}^{(n)}$ . At this point, the amplitude of the focal field is substituted with a weighted sum of the target amplitude and the focal field amplitude itself. The resulting field is inverse Fourier transformed, obtaining  $E_{\text{inv}}^{(n)}$ . Finally, the hologram phase is updated to the phase of  $E_{\text{inv}}^{(n)}$ . If the focal intensity and the target intensity differ more than an acceptable error, the cycle is then repeated (until a certain maximum number of iterations is reached).

uniformity over all the traps in the array. In the benchmark test we present in Table 11.1, we obtained  $I_{\text{tot}} = 0.93$  and  $u = 0.99$  after 30 iterations.

**Exercise 11.2.15** Implement the adaptive-additive algorithm and study its performance.

### 11.2.6 Direct search algorithms

The holograms obtained with the previous algorithms can be refined by *direct search algorithms* where a *gain function* is defined and optimised. For example, we can choose a gain function obtained as a linear combination of the average intensity [Eq. (11.25)] and percentage standard error metrics [Eq. (11.27)], i.e.,

$$F_{\text{gain}} = \langle I \rangle - w\sigma, \quad (11.30)$$

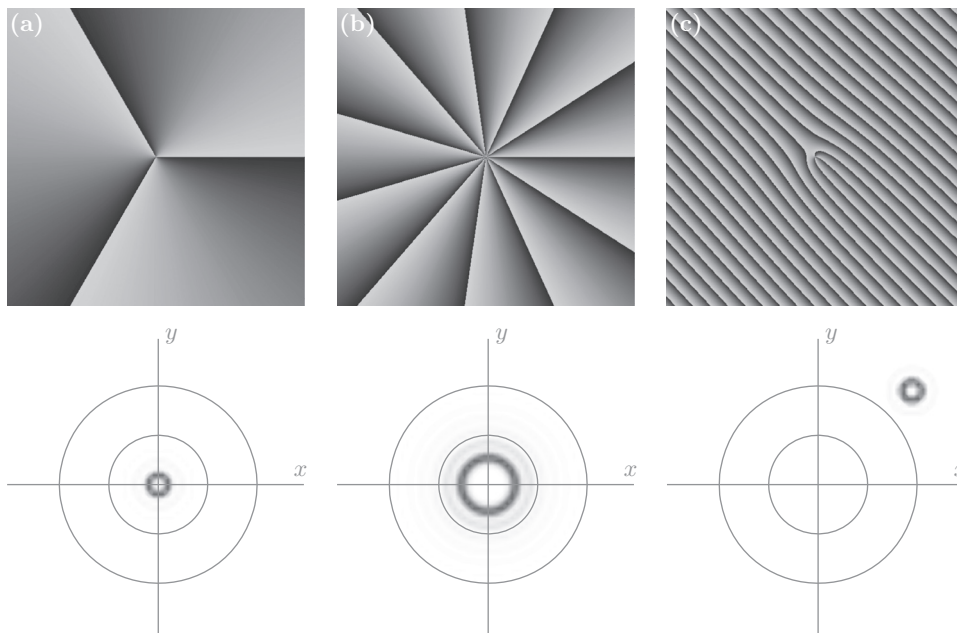
which is a function of all  $\phi_{m_x, m_y}$  where  $w$  is a weighting factor. Then, starting from a good initial guess for the hologram, obtained using one of the algorithms explained above, a pixel is picked at random and cycled through all its possible grey levels while looking for an increase of  $F_{\text{gain}}$ . In this way, it is possible to improve the uniformity and efficiency of the hologram and to adjust the relative importance of the two by tuning  $w$  (typically  $0 < w \leq 1$ ). Further improvements can be obtained by allowing for moves that temporarily decrease the gain (as in Monte Carlo algorithms) in a process known as *simulated annealing*.

**Exercise 11.2.16** Any given optical field propagating through an optical system can be expressed as a composition of modes in an arbitrary orthogonal representation (e.g., orthogonal plane waves). Show that optimal focusing is achieved if all the modes meet at a selected point in space with the same phase and suggest a method to achieve this using a DOE and a direct search algorithm. [Hint: You can follow the method proposed by Čižmár et al. (2010).]

**Exercise 11.2.17** How can the DOE be used in order to correct aberrations present in the optical system in order to achieve a more tight focus and, thus, more efficient optical traps? [Hint: For example, try adding (modulo  $2\pi$ ) Zernike polynomials to the original hologram.]

## 11.3 Higher-order beams and orbital angular momentum

Until now, we have only considered how to realise arrays of traps generated by Gaussian beams. Another powerful area that can be accessed using wavefront engineering is that of non-Gaussian beams. Here, we describe the techniques that permit one to generate, in particular, Hermite–Gaussian beams, Laguerre–Gaussian beams and non-diffracting beams, which we have described in detail in Subsections 4.4.2, 4.4.3 and 4.4.4, respectively. These beams can be straightforwardly generated starting from a uniform phase profile by

**Figure 11.6**

Laguerre–Gaussian beam. The beam can be generated by the phase modulation given by Eq. (11.31) and shown in (a) and (b) for beams of azimuthal order  $l = 3$  and  $11$ . Note that there are exactly  $l \cdot 2\pi$  phase jumps along the angular direction. In (c), a grating is added to the phase mask in (a) to alter the direction of the 1st-order Laguerre–Gaussian beam away from the 0th-order unmodulated light. Both the phase modulation (top) and the focal spot intensity (bottom) are shown.

projecting onto the DOE their own characteristic phase profile, which we have seen in Figs. 4.7, 4.8 and 4.9, respectively. For example, the phase profile of a Laguerre–Gaussian beam of orders  $p$  and  $l$  at the beam waist  $w_0$  can be obtained from the expression of the beam in Eq. (4.28) as

$$\phi(\rho, \varphi) = il\varphi + \pi \Theta \left\{ L_p^l \left( 2 \frac{\rho^2}{w_0^2} \right) \right\}, \quad (11.31)$$

where  $\Theta \{ \cdot \}$  is the Heaviside step function. The azimuthal order causes  $l \cdot 2\pi$  phase jumps along the angular direction. The radial order  $p$  leads to  $p + 1$  radial regions, whose borders correspond to the  $p$  zeros of the corresponding generalised Laguerre function. It is typically convenient to shift the generated Laguerre–Gaussian beam away from the unmodulated 0th-order beam by adding a blazed grating to the phase modulation mask, as shown in Fig. 11.6 and explained in Section 11.5.

**Exercise 11.3.1** Simulate the generation of Laguerre–Gaussian beams using a phase mask.  
[Hint: You can adapt the program `slmlg` from the book website.]

**Exercise 11.3.2** Show that a Hermite–Gaussian beam of orders  $m_x$  and  $m_y$  can be generated using the phase modulation

$$\phi(x, y) = \Theta \left\{ H_{m_x} \left( \sqrt{2} \frac{x}{w_0} \right) H_{m_y} \left( \sqrt{2} \frac{y}{w_0} \right) \right\}. \quad (11.32)$$

Simulate its generation using an appropriate phase mask. [Hint: Start from Eq. (4.25). For the simulation, you can adapt the program `slmlg` from the book website.]

**Exercise 11.3.3** How can Bessel beams and non-diffracting beams be generated using a phase mask? [Hint: Peruse Subsection 4.4.4 and Rose et al. (2012).]

**Exercise 11.3.4** How can multiple Laguerre–Gaussian beams be generated in order to produce the counter-rotating optical traps shown in Fig. 11.1?

## 11.4 Continuous optical potentials

Wavefront engineering can also be employed to generate continuous optical potentials. In fact, the Gerchberg–Saxton and adaptive-additive algorithms, which we have seen in Subsections 11.2.4 and 11.2.5, respectively, are ideally suited to obtain phase profiles capable of generating continuous intensity distributions. The main difference regards the definition of the criterion employed to define the quality of the generated phase profile. In order to evaluate the convergence and to be able to impose a stop criterion, the resulting modulus of the complex amplitude of the scalar field at the focal plane is compared to the desired one,

$$C = \iint [A_{\text{focus}}(x, y) - A_{\text{target}}(x, y)]^2 dx dy, \quad (11.33)$$

where  $A_{\text{focus}}(x, y)$  is the electric field intensity at the focal plane and  $A_{\text{target}}(x, y)$  is the target intensity. The loop is iterated until the stop criterion is met, i.e., either a maximum number of iterations or a threshold error is reached.

Finally, we note that the same algorithm can be also applied to obtain a continuous distribution in multiple planes.<sup>3</sup> The algorithm, which generalises the ones presented in Figs. 11.4 and 11.5, is as follows:

1. propagate the field at the DOE to the multiple planes;
2. calculate the total error as the sum of the error calculated at each plane per Eq. (11.33);
3. inverse-Fourier transform these fields, multiply them by the inverse lens factor and add all contributions;
4. replace the amplitude at the DOE plane with the imposed one;
5. iterate this loop until the stop criterion is met.

<sup>3</sup> A generalisation to full three-dimensional shaping is currently far too slow for interactive use, taking days to calculate the desired phase modulation (Shabtay, 2003; Whyte and Courtial, 2005). Nevertheless, as described in Box 11.2, future improvement of GPU performance holds the promise that this will be soon feasible within reasonable time scales.



## Box 11.2

## GPU computation of holograms

Unlike the central processing unit (CPU), which consists of a few cores optimised for sequential serial processing, the graphics processing unit (GPU) is designed for parallel processing of simultaneous operations on thousands of cores. To exploit the capabilities of the GPU and enable parallelisation of computation, NVIDIA has introduced the complete unified device architecture (CUDA). By optimising the code as explained, e.g., by Bianchi and Di Leonardo (2010), it is possible to achieve the calculation of holograms hundreds of times faster than on the CPU. Furthermore, Haist et al. (2006) cite other advantages of using the GPU, including increased performance per unit cost, ease of upgrading graphics boards and the expectation that the rate of increase in GPU performance (driven by the demand for ever more realistic computer game graphics) will continue to outstrip that in CPU performance. Potential drawbacks include the complexity of optimisation of code, which may also then need to be re-optimised for different GPUs, the consequent lack of flexibility and possibly even a reduction in speed if large amounts of data are transferred to the GPU, negating its advantage.

**Exercise 11.4.1** Write a code to generate continuous optical potentials using the Gerchberg–Saxton algorithm both on a single plane and on multiple planes.

**Exercise 11.4.2** Show that, when the Gerchberg–Saxton algorithm is used to generate a continuous optical potential, the error as defined by Eq. (11.33) diminishes or stays the same for each iteration. [Hint: Read the article by Fienup (1982).]

**Exercise 11.4.3** Write a code to generate continuous optical potentials using the adaptive-additive algorithm both in a single plane and in multiple planes.

## 11.5 Set-up implementation

The configurations most commonly employed to actually build a holographic optical tweezers (HOT) are illustrated in Fig. 11.7. In the scheme presented in Fig. 11.7a, starting from the configuration described in Section 11.1 and illustrated in Fig. 11.2a, the DOE plane is optically conjugated to the back focal plane of the optical tweezers objective, so that the complex amplitude at the trapping plane, i.e., the front focal plane of the objective, is the Fourier transform of the complex amplitude in the DOE plane. Therefore, optical conjugation is achieved by positioning the DOE in the input plane of a telescope whose role is to project the hologram onto the input pupil of the objective lens. To calculate the effective displacement of the optical trap in the objective front focal plane, one has to consider the optical train after the DOE, which typically consists of a telescope and the microscope objective. Because the telescope magnifies the DOE field by a factor  $s$ , which is equal to the ratio of the focal lengths of its lenses, the grating period imaged by this telescope is equal to  $s\Lambda$  and the angle of the 1st-order diffraction on the back focal plane of the microscope objective is scaled by a factor of  $1/s$  to  $\alpha/s$ . Therefore, the displacement

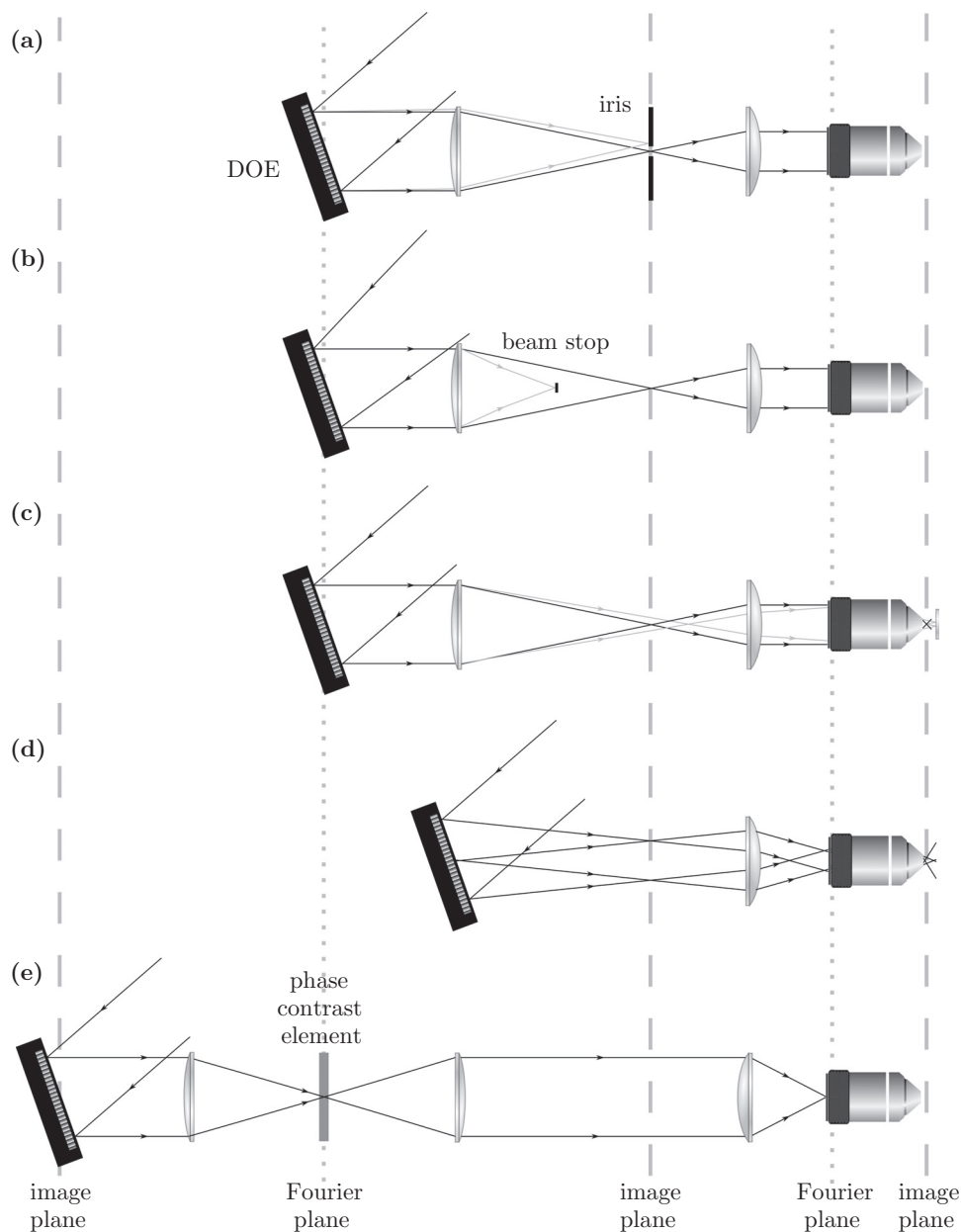


**Figure 11.7** HOT configurations. Holographic optical tweezers (HOTs) can be configured in different ways. (a) The spatial light modulator (SLM) can be positioned exactly in the Fourier plane and the 1st-order diffracted beam can be deflected away from the 0th-order beam and spatially selected using an iris, or (b) close to the Fourier plane to allow the 0th-order beam to be removed with a spatial filter (beam stop). (c) A counter-propagating optical trapping configuration can be generated by placing a mirror behind the sample plane, allowing for the use of objectives with lower numerical apertures and longer working distances. Furthermore, the SLM can also be placed (d) in a Fresnel plane or (e) in a plane conjugated to the image plane, e.g., to use the phase contrast approach discussed in Subsection 11.6.2.

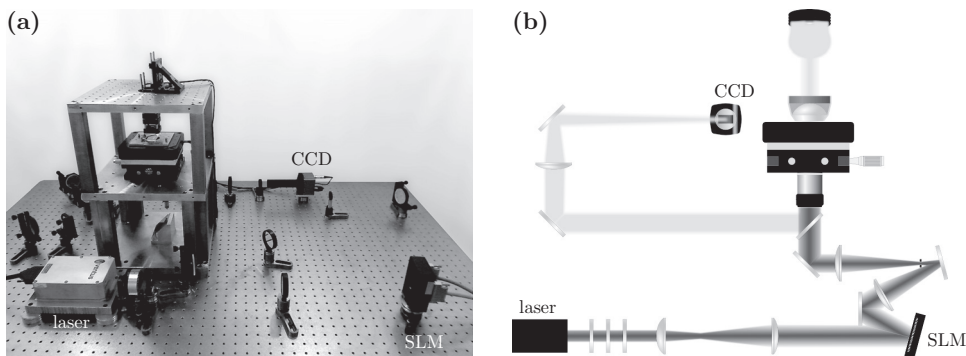


**Figure 11.8** HOT set-up. (a) Holographic optical tweezers (HOT) set-up and (b) corresponding schematic.

of the beam in the front focal plane of the objective is

$$u = f_{\text{OBJ}} \frac{\lambda_0}{s \Lambda}, \quad (11.34)$$

where  $f_{\text{OBJ}}$  is the objective focal length. Analogous considerations apply to the effect of a Fresnel lens. We note that although Eq. (11.9) provides a first approximation to the field in the focal plane of the objective, some deviations arise because of the high numerical aperture of the objective and the exact focal field can be calculated using the focusing theory explained in Section 4.5.

The HOT set-up we will build is shown in Fig. 11.8. Starting from the optical tweezers we realised in Chapter 8, we removed the laser and build a new optical train with a 4f-configuration in order to add a DOE, which in our case is a reflective spatial light modulator (SLM). One important technical detail is that the SLM is arranged so that the 0th-order beam, i.e., the beam simply reflected by the SLM, is reflected in a direction different from that of the optical train of the optical trap; i.e., it is made to point to the side and downwards (for laser safety). Consequentially, we need to project a diffraction grating onto the SLM in order to generate a 1st-order beam aligned along the optical train of the optical trap for the following alignment procedure; an iris placed in the intermediate focal plane can help in removing the residual components of the 0th-order, as shown in Fig. 11.7a.<sup>4</sup> Then we can proceed to align the system as discussed in Section 8.4. Finally, we can place our sample on the stage and start our holographic optical trapping adventure on the lines of what we did in Section 8.5, but without the need for moving the sample. After a particle has been trapped, it is possible to move the trap vertically by adding a Fresnel lens to the computer-generated hologram: the optically trapped particle will get out of focus, whereas the non-optically-trapped particles on the sample cell bottom remain in focus. It is also possible to move the trap laterally by adding a blazed grating: the image of the optically trapped particle will move within the field of view of the camera, whereas the background

<sup>4</sup> An alternative approach to removing the 0th-order beam is to use a slightly convergent beam and to place a beam stop before the intermediate focus, as shown in Fig. 11.7b. In fact, as the focus of the incoming beam lies before the intermediate focal plane, the 0th-order beam can easily be removed by a spatial filter, e.g., a glass slide with a microfabricated reflecting or absorbing dot.

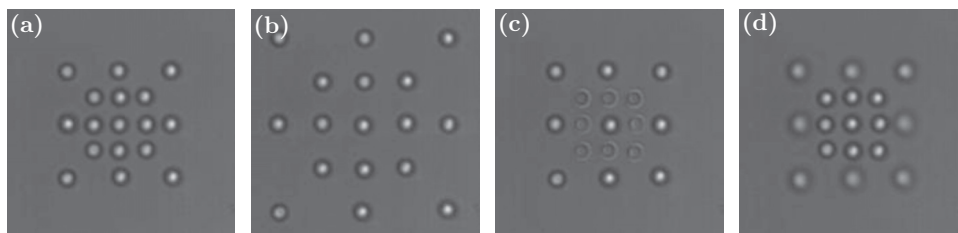


**Figure 11.9** Holographically optically trapped particles. An array of holographic optical traps is used (a) to trap 17 particles, (b) to move them laterally in the focal plane and (c), (d) to move them vertically in the direction perpendicular to the focal plane.

particles sedimented on the coverslip will appear to remain in the same position. Of course, at this point, the interesting part of using HOTs is to create multiple reconfigurable traps, as shown in Fig. 11.9, or non-Gaussian traps, as shown in Fig. 11.1.

Some other configurations are also possible. For example, a counter-propagating beam trap can be generated in a set-up where the sample cell has a reflecting surface: two beams with different curvatures, and thus different axial focal positions, can be generated by the SLM and employed as two counter-propagating beams, as schematically shown in Fig. 11.7c. Such systems can employ lower NA than conventional three-dimensional traps and thus feature a longer working range.

One is not restricted to using the SLM in the Fourier plane. Indeed, it is also possible to use it in an intermediate Fresnel or image plane. Positioning the SLM in an intermediate Fresnel plane, as shown in Fig. 11.7d, simplifies the hologram design in that the SLM aperture can be divided into different trap regions so that moving the position of one of the traps slightly is simply accomplished by translating the corresponding section of the SLM pattern, which is computationally quick. Positioning the SLM in an image plane, as shown in Fig. 11.7d, permits one to directly image the image projected onto the SLM to the optical trap plane; this is computationally very efficient, even though it can lead to greater losses than phase-only modulation.

In all configurations, the calculation of the optimum hologram for a large number of optical traps or for multiple-plane continuous optical potentials is a computationally intensive task. These limitations become particularly evident in applications where real-time and interactive optical manipulation (see, e.g., Subsection 12.6) is required, as even optimised algorithms may not perform fast enough and thus may be limited to running pre-calculated series of holograms to steer the optical traps along pre-defined paths. A possible approach to overcoming this problem is shifting the intensive parts of the computation to the graphics processing unit (GPU) in order to exploit its parallel architecture, as explained in Box 11.2.

### 11.5.1 Spatial light modulators

A spatial light modulator (SLM) is a device that functions as a DOE by control of either the amplitude or the phase of an optical beam in a plane transverse to the direction of propagation. Amplitude modulators (which include digital micromirror devices) obviously

have a lower diffraction efficiency for transformation of the input beam into the desired pattern for optical trapping, because a significant proportion of the input beam is simply blocked or directed away from the path of the trapping beam. Phase modulators, which are available in both transmissive and reflective forms, use a pixellated liquid crystal display to imprint a spatially varying pattern that ideally alters only the phase via the change in refractive index associated with the reorientation of the liquid crystal under an applied voltage. In a transmissive SLM, the beam passes once through the liquid crystal layer (and its supporting substrate). In a reflective SLM (commonly known as liquid crystal on silicon, or LCoS), the beam passes through the liquid crystal, reflects from the substrate and then passes through the liquid crystal again. This means that a reflective SLM can employ a thinner liquid crystal layer to achieve the same phase retardation, which can result in an increase in the switching speed (which varies as the square of the layer thickness). Liquid crystal-based technologies have the advantage of being relatively advanced, being lower in cost, and having shorter switching times.<sup>5</sup>

Two distinct classes of liquid crystal SLMs based on the type of liquid crystal used should be considered. Ferroelectric liquid crystal SLMs can switch between only two phase retardation levels (0 and  $\pi$ ), which limits diffraction efficiency, but are capable of fast switching speeds of up to 1 kHz. The more common nematic liquid crystal SLMs approximate continuous phase variation with a large number (typically 256) of discrete retardation levels from 0 up to the maximum dynamic range of the device – most often  $2\pi$ , although modulators which produce a greater than  $2\pi$  maximum retardance are available. Nematic liquid crystal SLMs typically switch at video frame rate, i.e., 60 Hz.

Other factors to consider when selecting a suitable spatial light modulator for optical tweezers applications may include

- **Pixel size and number.** These will affect the resolution of, for example, positioning of a trap in the transverse plane. Currently LCoS SLMs with a pixel pitch as small as 6.4  $\mu\text{m}$  and up to  $1920 \times 1080$  pixels are available.
- **Pixel filling factor.** This refers to the area of the display taken up by the liquid pixel crystals: a higher filling factor reduces the inactive region between pixels, thereby increasing the efficiency of conversion into the phase modulated beam. For most devices a filling factor over 80% is specified.
- **Wavelength range.** Ideally the SLM will be anti-reflection coated at the laser wavelength to be employed and capable of at least  $2\pi$  retardation. Models for wavelength ranges from the blue end of the visible spectrum to telecom (near-infrared) wavelengths are available.
- **Phase resolution.** Greyscale resolution is typically 8-bit (256 levels), although SLMs with 12-bit resolution are already available.
- **Polarisation sensitivity.** Standard LCoS SLM devices will apply the phase modulation to one direction of linear polarisation only; however, polarisation-independent SLMs have recently been introduced.

<sup>5</sup> Manufacturers of liquid crystal spatial light modulators currently available include Boulder Nonlinear Systems (USA) (now part of Meadowlark Optics), HoloEye Photonics (Germany), Hamamatsu (Japan) and Jenoptik (Germany).

- **Damage threshold.** When using high-power or pulsed lasers care should be taken not to exceed the maximum power density that would avoid damage to the liquid crystal layer.

## 11.6 Alternative approaches

Several alternative approaches are available to generate large arrays of optical traps. For example, as discussed in Subsections 4.4.4 and 12.2, using multi-beam interference (discrete beams) is simple, produces high-quality optical lattices over extended three-dimensional volumes and can tolerate high beam powers. However, such approaches are limited to (quasi-)symmetric patterns. Alternatively, galvo-mirrors or piezoelectrics have served as the basis for designs involving scanning laser tweezers, building on the approach described in Subsection 8.5.1. Another (DOE-based) strategy that allows flexible generation of trap arrays uses the *generalised phase-contrast* (GPC) method. In addition, arrays covering large areas have now been produced using evanescent waves. In the remainder of this section, we will discuss the time-shared optical trap approach [Subsection 11.6.1] and the GPC approach [Subsection 11.6.2]; evanescent trapping will be discussed in Section 12.4.

### 11.6.1 Time-shared optical traps

Multiple time-shared optical traps can be obtained using several beam steering techniques and a 4f configuration, such as the one described in Subsection 8.5.1. The laser needs to be repositioned on a time scale short enough so that the trapped particles experience only a time-averaged potential. Two of the most commonly employed devices are acousto-optic deflectors (AODs) and galvo-mirrors. AODs create a blazed grating by generating acoustic standing waves within a crystal and thus creating a periodic alteration of the crystal's refracting index so that a light beam can be deflected in one direction; using two such crystals, it is possible to deflect a beam in two directions ( $x$  and  $y$ ). The main advantage of AODs over SLMs, is that they can be scanned at hundreds of kilohertz.<sup>6</sup> Galvo-driven mirrors can be controlled by an electro-optical modulator, which can yield smoothly varying intensity modulations in a continuous optical potential. In applications where a smooth potential is required, such as in the creation of a smooth ring trap (Blickle et al., 2007), galvo-mirrors might be preferred over either HOTs or AODs because they provide a much higher throughput of the incident light than either AODs or Fourier-plane HOTs; however, inertia limits the scan speed of any macroscopic mirror to a fraction of what is available via AODs. Unlike the SLM-based techniques, systems based on AODs

<sup>6</sup> Some technical issues need to be accounted for when working with AODs. In particular, ghost traps might appear in analogue AOD systems (as the beam is often sequentially repositioned in  $x$  and then in  $y$ , so the generation of two traps along the diagonal of a square yields an unintended spot at one of the other corners). Furthermore, as the AOD efficiency falls off as a function of the deflection angle, for applications requiring uniform arrays, one must compensate, either by spending more time at peripheral traps or by increasing the power sent to those traps. Finally, AOD-generated arrays can be thought of as being made up of incoherent light (different beams do not interfere, being present only one at a time).

and galvo-mirrors cannot normally do mode conversion or aberration correction, and they cannot generate three-dimensional arrays of traps.

In all time-shared optical trapping techniques, in order for each trapped particle to feel only the time-averaged potential, the maximal time that the laser can spend away from any one trap needs to be much smaller than the characteristic time it takes the particle to diffuse across the trap, i.e., the time scale  $\tau_c = 1/f_c$ , where  $f_c$  is the corner frequency in the power spectrum [Section 9.8]. In fact, while the trap is not at the site, the particle diffuses away from its nominal trapping site by a characteristic distance  $d = \sqrt{6Dt_{\text{off}}}$ , where  $D$  is the particle diffusion coefficient and  $t_{\text{off}}$  is the time the laser is off at the site. For example, for a 1  $\mu\text{m}$  radius particle in water and  $t_{\text{off}} = 1$  ms, we can expect an average diffusion of  $d = 36$  nm. Clearly, the smaller the particle, the shorter  $\tau_c$  becomes; also, the less viscous the medium, the shorter  $\tau_c$ .<sup>7</sup> This, together with the requirement that the laser spends sufficient time at each trap site to produce the time-averaged power required for the desired trap strength and the fact that, although trap strength depends only on the time-average power, sample damage due to two-photon absorption and local heating contain a dependence upon the peak power, limits both the type of arrays that can be constructed and the accuracy to which the spheres can be positioned using time-shared trapping.

### 11.6.2 Generalised phase contrast

Another alternative approach positions the SLM in the image plane of the traps, as shown in Fig. 11.7e. This method, known as the *generalised phase-contrast* (GPC) technique, was developed by Mogensen and Glückstad (2000), building on the phase contrast imaging method developed by Frits Zernike, which we discussed in Subsection 8.2.2. In this configuration, the SLM acts as a phase-contrast element where a phase pattern displayed on the SLM produces the same intensity distribution in the sample plane and, thus, complicated distributions of traps can be produced without any need for sophisticated computing. As opposed to a simple intensity mask, which creates the desired pattern by blocking the unwanted light, phase contrast is optically efficient, ensuring that all of the laser light is directed into the optical traps; in fact, this set-up can reach a much higher modulation efficiency (up to 90%) without speckle noise or ghost traps. Because, in the GPC approach, the SLM is conjugate to the trapping plane, no computations are required to convert the phase-only modulation of the SLM into an intensity modulation in the image plane; instead there is a direct, one-to-one correspondence between the phase pattern displayed on the SLM and the intensity pattern created in the trapping plane. In the Fourier plane, a small  $\pi$ -phase filter shifts the focused light coming from the SLM so that at the image plane it will interfere with a plane-wave component. The result is a system that only requires the user to write the desired two-dimensional patterns on the SLM. The downside to this

<sup>7</sup> This practically means that when particles are being trapped in air, as we will discuss in Chapter 19, the corner frequency can reach value of several kilohertz even for large (several micrometre) radius particles. This is an issue that, in fact, has limited the application of time-shared techniques to the trapping of aerosols, leaving the use of HOTs as a preferable choice.



is that  $xy$ -positions are limited to pixel positions, meaning that ultra-high-precision trap positioning is not possible to the degree it is with the other SLM-based techniques.

Extension of the GPC method to three dimensions requires the use of counter-propagating beam traps, rather than optical tweezers, and, therefore, three-dimensional control is, in some sense, more involved. For this reason, Dam et al. (2007) have developed an automated alignment protocol for users interested in three-dimensional control. Nevertheless, it is not possible to place traps behind each other controllably with this method, but there are now many impressive demonstrations of three-dimensional manipulation using the GPC technique, e.g., in some of the applications described in Chapter 16. The version of GPC using counter-propagating beam traps can also use low-NA optics, which can have a large field of view and a large Rayleigh range. So, although Fourier-plane holographic optical traps can provide only a small range of axial displacements, limited by spherical aberration, the low-NA GPC trap arrays are sometimes called *optical elevators* because of the wide range over which the traps can be displaced along the optical axis, as the working distance can be up to 1 cm, which is roughly 100 times that of a conventional optical tweezers set-up.

## Problems

- 11.1 *Genetic algorithms.* Develop a program that uses genetic algorithms to generate holograms to produce arrays of optical traps and optical trapping potentials. Compare the performance of these algorithms with that obtained using the algorithms described in the text.
- 11.2 Calculate the phase and intensity structure of two optical vortices with the same vorticity but located at opposite positions within a Gaussian profile. Study (experimentally or by simulations) the evolution when the positions get closer to the optical axis until merging. Does the total vorticity of the beam change as vortices move towards the higher intensity region? What happens if the two vortices possess opposite charges?
- 11.3 *Fractional optical vortices.* Laguerre–Gaussian beams possess a phase structure that yields a perfect helicoidal phase front only for integer  $l$ . Following the work of Berry (2004), investigate theoretically the phase structure of beams that possess fractional  $l$  values and show that they have a complex phase structure comprising many vortices at different locations within the beam cross-section. Design an SLM-based set-up and the corresponding holograms needed to study these fractional optical vortices. Compare your experimental (or simulated) results for different fractional values of  $l$  with those of Leach et al. (2004) and Lee et al. (2004).
- 11.4 *Interferometric synthesis of cylindrical vector beams.* Design a set-up that can generate cylindrical vector beams interferometrically with one SLM that works either in transmission or in reflection. Consider first a design that has a 4f configuration



and describe the holographic pattern you need to transfer to the SLM to generate radially and azimuthally polarised beams. Then consider a design that includes a Sagnac interferometer. What are the advantages and disadvantages of the two configurations? How can you synthesise fractional cylindrical vector beams? Suppose you use a reflection SLM that needs to be used at small reflection angles. How can you modify the Sagnac interferometer to avoid right angle reflection at the SLM? Compare your designs with those of Maurer et al. (2007) and Jones et al. (2009).

## References

- Berry, M. V. 2004. Optical vortices evolving from helicoidal integer and fractional phase steps. *J. Opt. A Pure Appl. Opt.*, **6**, 259–68.
- Bianchi, S., and Di Leonardo, R. 2010. Real-time optical micro-manipulation using optimized holograms generated on the GPU. *Comp. Phys. Commun.*, **181**, 1444–8.
- Blickle, V., Speck, T., Lutz, C., Seifert, U., and Bechinger, C. 2007. The Einstein relation generalized to non-equilibrium. *Phys. Rev. Lett.*, **98**, 210601.
- Čižmár, T., Mazilu, M., and Dholakia, K. 2010. *In situ* wavefront correction and its application to micromanipulation. *Nature Photon.*, **4**, 388–94.
- Dam, J. S., Rodrigo, P. J., Perch-Nielsen, I. R., Alonzo, C. A., and Glückstad, J. 2007. Computerized “drag-and-drop” alignment of GPC-based optical micromanipulation system. *Opt. Express*, **15**, 1923–31.
- Dufresne, E. R., Spalding, G. C., Dearing, M. T., Sheets, S. A., and Grier, D. G. 2001. Computer-generated holographic optical tweezer arrays. *Rev. Sci. Instrumen.*, **72**, 1810–16.
- Fienup, J. R. 1982. Phase retrieval algorithms: A comparison. *Appl. Opt.*, **21**, 2758–69.
- Gerchberg, R. W., and Saxton, W. O. 1972. A practical algorithm for the determination of the phase from image and diffraction plane pictures. *Optik*, **35**, 237–46.
- Haist, T., Reicherter, M., Wu, M., and Seifert, L. 2006. Using graphics boards to compute holograms. *Comput. Sci. Eng.*, **8**, 8–13.
- Jones, P. H., Rashid, M., Makita, M., and Maragò, O. M. 2009. Sagnac interferometer method for synthesis of fractional polarization vortices. *Opt. Lett.*, **34**, 2560–62.
- Leach, J., Yao, E., and Padgett, M. J. 2004. Observation of the vortex structure of a non-integer vortex beam. *New J. Phys.*, **6**, 71.
- Lee, W. M., Yuan, X.-C., and Dholakia, K. 2004. Experimental observation of optical vortex evolution in a Gaussian beam with an embedded fractional phase step. *Opt. Commun.*, **239**, 129–35.
- Maurer, C., Jesacher, A., Fürhapter, S., Bernet, S., and Ritsch-Marte, M. 2007. Tailoring of arbitrary optical vector beams. *New J. Phys.*, **9**, 78.
- Mogensen, P. C., and Glückstad, J. 2000. Dynamic array generation and pattern formation for optical tweezers. *Opt. Commun.*, **175**, 75–81.
- Rose, P., Boguslawski, M., and Denz, C. 2012. Nonlinear lattice structures based on families of complex nondiffracting beams. *New J. Phys.*, **14**, 033018.

- Shabtay, G. 2003. Three-dimensional beam forming and Ewald's surfaces. *Opt. Commun.*, **226**, 33–7.
- Whyte, G., and Courtial, J. 2005. Experimental demonstration of holographic three-dimensional light shaping using a Gerchberg–Saxton algorithm. *New J. Phys.*, **7**, 117.